

Analytical model of the fundamental mode of 3D square split ring resonators

Cite as: J. Appl. Phys. **125**, 014901 (2019); <https://doi.org/10.1063/1.5053482>

Submitted: 23 August 2018 . Accepted: 10 December 2018 . Published Online: 02 January 2019

Andrea Vallecchi , Ekaterina Shamonina, and Christopher J. Stevens



View Online



Export Citation



CrossMark

ARTICLES YOU MAY BE INTERESTED IN

[Phonon properties and thermal conductivity from first principles, lattice dynamics, and the Boltzmann transport equation](#)

Journal of Applied Physics **125**, 011101 (2019); <https://doi.org/10.1063/1.5064602>

[Excitation of graphene magneto-plasmons in terahertz range and giant Kerr rotation](#)

Journal of Applied Physics **125**, 013102 (2019); <https://doi.org/10.1063/1.5057372>

[Perspective: Nanoscopy of charge kinetics via terahertz fluctuation](#)

Journal of Applied Physics **125**, 010901 (2019); <https://doi.org/10.1063/1.5079534>

Applied Physics Reviews
Now accepting original research

2017 Journal
Impact Factor:
12.894



Analytical model of the fundamental mode of 3D square split ring resonators

Cite as: J. Appl. Phys. **125**, 014901 (2019); doi: [10.1063/1.5053482](https://doi.org/10.1063/1.5053482)

Submitted: 23 August 2018 · Accepted: 10 December 2018 ·

Published Online: 2 January 2019



Andrea Vallecchi,^{a)}  Ekaterina Shamonina, and Christopher J. Stevens

AFFILIATIONS

Department of Engineering Science, University of Oxford, Parks Road, Oxford OX1 3PJ, United Kingdom

^{a)} Author to whom correspondence should be addressed: andrea.vallecchi@eng.ox.ac.uk

ABSTRACT

An analytical model is developed for the charge and potential distributions of the fundamental mode of three-dimensional (3D) singly split ring resonators (SRRs) with square cross section, which nowadays can be conveniently fabricated by additive manufacturing techniques. This model allows the derivation of approximate formulas for the equivalent capacitance and the analysis of the resonant properties of this type of SRRs at any frequency. The total capacitance is expressed as the sum of the usual gap capacitance and a surface capacitance associated with the charges on the SRR walls, which are determined from the solution for the irrotational part of the electric field of a square split cylinder obtained by conformal mapping. The applicability of the proposed model for a broad range of SRR parameters is demonstrated by comparing the resonance frequency of sample SRR configurations found theoretically with the corresponding values obtained by numerical simulations and experiments. Furthermore, the functions describing the charge and current mode profiles provided in this work can be instrumental in estimating the near-field interaction and the coupling constants of an ensemble of resonant 3D square split rings and thus for tailoring the response of metamaterials and other devices formed by these elements.

© 2019 Author(s). All article content, except where otherwise noted, is licensed under a Creative Commons Attribution (CC BY) license (<http://creativecommons.org/licenses/by/4.0/>). <https://doi.org/10.1063/1.5053482>

I. INTRODUCTION

Design and fabrication of metamaterials at all scales, from microwaves to optical frequencies, has hitherto largely concentrated on planar structures, and the majority of devices have been demonstrated for specific polarizations and propagation directions. However, the advent and fast advancement of additive manufacturing technology has recently made available a new generation of three-dimensional (3D) printing techniques and materials that support the realisation of composite geometries including both metals and dielectrics for antennas and metamaterial designs by means of low-cost commercial desktop printers.^{1–4} Additive manufacturing can have the potential to meet the requirements of 3D electromagnetic designs incorporating non-planar complex geometries and inhomogeneous materials.⁵ Specifically, raised versions of the planar resonant elements usually used in filters and metamaterials can be easily realized, of virtually any height, by 3D printing, and this additional geometrical degree of freedom fosters the

development of a wealth of new structures with enhanced characteristics.^{6,7}

Split-ring resonators (SRRs) are one of the basic inclusions for the realization of metamaterials.⁸ In this context, although several different SRR configurations have been investigated, the most conventional ones are certainly circular and rectangular SRRs.^{9–12} In particular, rectangular SRRs can be more advantageous than circular resonators to achieve higher miniaturization, denser packing,^{12,13} and stronger magnetic coupling.¹⁴ Moreover, square and rectangular SRR geometries are simple to make, and for this reason, they have been extensively used in left-handed and magnetic metamaterials at microwave and THz frequencies.^{15,16} Recently, it has also been shown that 3D square SRRs with a finite height can exhibit significantly stronger coupling compared to the fully planar structures with the same footprint and that the coupling coefficient steadily increases for increasing height of the resonators; this trend can be exploited for designing devices featuring either

wider operating bandwidths or miniaturized layouts without performance degradation.¹⁷

Quasi-static methods have been proposed to estimate the resonance frequency and magnetic polarizability of planar SRRs in different configurations, which are the most relevant parameters for the design of metamaterials.^{18–20} In this work, the focus is on the development of an analytical model to characterise the fundamental mode of metallic 3D raised singly split square ring resonators, and especially on the derivation of an approximate expression of their equivalent capacitance to then predict their resonance properties. As shown in Ref. 10 for the case of circular split rings, the capacitance of a split ring is not only due to the gap, which essentially forms a parallel-plate capacitor whose capacitance can be easily calculated, but the charges on the ring walls also play a role providing an additional surface capacitance. To derive the surface capacitance of 3D square SRRs, we will refer to the corresponding 2D case of an infinite cylindrical structure with the same cross section, for which the irrotational part of the electric field and the associated potential distribution produced by a voltage applied to the gap is found by applying conformal mapping²¹ to the solution in a circular cylinder.²² In particular, the case of a cylinder with an infinitesimal gap is taken as a reference in the analytical developments, although the solution for a cylinder with a finite width of the gap could be similarly used with some added complexity, as discussed in Appendix A. The outcome of this analysis is the potential and linear charge distributions in a cross section of the SRRs which are used to obtain an approximate expression of the capacitance of the SRRs and then, since formulas for the equivalent inductance of a ring of arbitrary shape are already available (see, e.g., Refs. 23 and 24), of their resonance frequency. For the reason of simplicity, in this work, we restrict ourselves to considering singly split resonators, yet the problem is linear, and the derived expressions can be extended to the case of multigap resonators by the principle of superposition and adding up the contributions associated with each gap.²⁵

It is noteworthy that within the model, both charge and current mode profile functions are proposed that can be employed to estimate the near-field interaction and the coupling constants of a collection of 3D square SRRs by the approach described in Ref. 26 and then extended in Refs. 27 and 28 to include the effect of retardation, which essentially consists of expressing the coupling parameters in terms of normalized electric and magnetic energies evaluable from the charge and current distributions. These functions can thus provide qualitative and quantitative information on the influence of the specific geometry and relative configuration of the split rings, identifying the relative contributions to the coupling of the electric and magnetic interactions, which can be crucial to effectively engineer the response of metamaterials, magnetoinductive wave arrays,²⁹ and filters formed by this type of SRRs. As long as the model neglects truncation effects in real finite split rings, it is expected that its accuracy will be poorer for thin resonators and progressively improve for longer more tubular structures.

The organization of the paper is as follows. The theoretical treatment is outlined in Sec. II, while part of the analytical details are provided in Appendixes A and B. Next, in the first part of Sec. III, the contributions of the gap and surface capacitances to the total capacitance will be compared, showing that generally the surface capacitance cannot be neglected. The validity of the proposed formulas will be tested by finding the resonance frequencies of the split rings predicted by the model and comparing with results of numerical simulations, in the second part of Sec. III, and the outcome of experiments in Sec. IV.

II. THEORETICAL MODEL

The geometry of the SRR with square cross section and a single gap is shown in Fig. 1(a). At the fundamental resonance, the SRR can be represented by the parallel LC equivalent circuit shown in Fig. 1(b), with the total capacitance consisting of the parallel connection of the capacitance of the gap (C_{gap}) and the surface capacitance (C_{surf}). This circuit layout can be heuristically explained by observing that the surface charge density is concentrated near the gap of an SRR, where the current instead remains negligible, and that, conversely, at the back of the SRR, on the side opposite to the gap, the surface charge becomes vanishingly small, while the current reaches its largest amplitude (see Figs. 4 and 9). Due to the small current in the region of the largest charge density, the voltage across the two capacitances is nearly identical, which justifies their parallel connection. Indeed, the distinction between the gap and surface capacitance is merely a modeling artifice to take into account the effect of the finite thickness of the conductor forming the SRRs. Further to this approximate physical picture, it could be shown that a more rigorous distributed model of the SRR reduces to the lumped equivalent circuit in Fig. 1(b) at the fundamental resonance, as done for the case of edge coupled singly split SRRs in Ref. 30. The aim of this work being to predict the SRR resonance frequency, its loss and radiation resistances are not considered in the circuit. Under these assumptions, which are analogous to those made in Ref. 10 for raised circular SRRs, the gap capacitance can be expressed as the parallel-plate capacitor of the gap that accounts for the fringing fields by increasing the linear dimensions of the plate spacing and

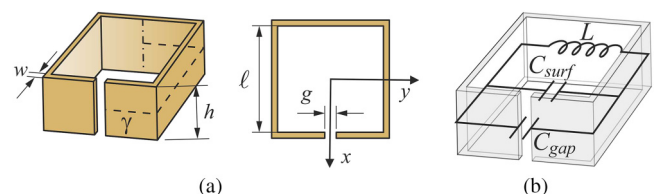


FIG. 1. (a) Geometry of 3D singly split ring resonator with square cross section and (b) its equivalent lumped LC circuit representation.

thickness as in Ref. 31

$$C_{gap} = C_{pp} + C_{fringe} = \epsilon_0 \left[\frac{(h+g)(w+g)}{g} \right]. \quad (1)$$

Next, we derive the expression of the surface capacitance. To begin with, the surface capacitance per unit height (p.u.h.) is defined as

$$C_{surf}^{p.u.h.} = \int_{\gamma} \frac{\rho(\gamma)}{V(\gamma)} d\gamma, \quad (2)$$

where ρ is the charge density and V is the voltage between two symmetric points on the surface of the ring. γ represents the curve corresponding to one half of the SRR cross section boundary, as shown in Fig. 1(a). Both the surface charge and the voltage in (2) can be obtained by referring to the infinitely long perfectly conducting cylindrical structure with the same cross section of the SRR and an infinitesimal gap, in analogy with the approach previously used to derive the capacitance of circular SRRs.¹⁰ The electric field in an infinite conducting cylinder has been found analytically in Ref. 22 starting by assuming that the voltage V_0 applied to its infinitesimal gap induces a uniform magnetic field inside the coil linked to V_0 by Lenz's law; then, the electric field is split into its solenoidal and irrotational parts; the former can be determined in terms of the magnetic field by using Faraday's law, it is purely azimuthal and independent of position, and thus clearly does not satisfy the boundary condition on the conducting surface of the cylinder; the irrotational part of the field must have a tangential component that cancels the solenoidal one and is expressed in terms of a scalar potential function which is the solution of the Laplace equation with the boundary condition corresponding to the vanishing of the total tangential electric field on the surface of the coil.²² In particular, the potential associated with the irrotational part of the electric field for a unit radius cylinder can be represented as

$$\Phi(r, \phi) = \frac{V_0}{\pi} \arctan\left(\frac{r \cos \phi - 1}{r \sin \phi}\right) + \frac{V_0}{2} \text{sign}(\pi - \phi). \quad (3)$$

Along the surface of the cylinder, Φ simply reduces to $\Phi(r=1, \phi) = V_0(\pi - \phi)/2\pi$, with $0 < \phi < 2\pi$.

The electric field in a conducting cylinder with square section is amenable to a similar decomposition. However, the knowledge of the irrotational part of the electric field, the only contributing to the charge density, and of the relative potential function suffice the purpose of determining the surface capacitance. In this respect, we recall that the 2D Laplace equation, which uniquely determines the electrostatic potential along with assigned boundary conditions on the domain of analysis, is invariant under an analytic mapping, i.e., if $U(\xi, \eta)$ satisfies the Laplace equation in the (ξ, η) variables, and $\zeta = \xi + j\eta = \xi(x, y) + j\eta(x, y) = g(z)$ is any analytic complex function, then the composition $u(x, y) = U[\xi(x, y), \eta(x, y)]$ also solves the Laplace equation in the (x, y) variables. As a consequence,

the potential in any point (x, y) of the cross section of a square cylinder with an arbitrary side length ℓ can be derived by the solution (3) for a circular domain by using the following conformal mapping of the unit disk onto a square of side ℓ based on the Schwarz-Christoffel formula²¹

$$z = x + jy = e^{-j\frac{\pi}{4}} \frac{4\ell\sqrt{\pi}}{\Gamma^2(1/4)} F(\zeta e^{j\frac{\pi}{4}}, j), \quad (4)$$

where $\zeta = \xi + j\eta = re^{j\phi}$ represents a point on the unit disk, $F(\zeta, k)$ denotes the incomplete elliptic integral of the first kind, and j is the imaginary unit. The inverse of the map (4) is the function

$$\zeta = e^{-j\frac{\pi}{4}} \text{sn}\left[ze^{j\frac{\pi}{4}} \frac{\Gamma^2(1/4)}{4\ell\sqrt{\pi}}, -1\right], \quad (5)$$

where $\text{sn}(z, k)$ is the Jacobi sine amplitude elliptic function,³² which maps a square of side ℓ onto the unit disk. The composition of (3) with the conformal map (5) provides the potential inside a conducting cylinder with a square cross section and along its boundary

$$u(z) = \frac{V_0}{\pi} \text{atan}\left\{ \frac{\text{Re}[\text{sn}(z', -1)] + \text{Im}[\text{sn}(z', -1)] - \sqrt{2}}{-\text{Re}[\text{sn}(z', -1)] + \text{Im}[\text{sn}(z', -1)]} \right\}, \quad (6)$$

where $z' = ze^{j\frac{\pi}{4}} \Gamma^2(1/4)/(4\ell\sqrt{\pi})$. From the knowledge of the potential (6), the electric field can be readily obtained as $\mathbf{E}_1 = -\nabla\Phi$. The detailed analytical calculations, though straightforward, are included in Appendix B for completeness. Next, the charge density can be obtained as $\rho(\gamma) = \epsilon_0 E_{1n}$, where ϵ_0 is the free space permittivity and E_{1n} is the component of the electric field normal to the surface of the resonator. Then, the coil surface capacitance p.u.h. can be calculated from (2), where the voltage V can be obtained, by either directly evaluating (6) on the square SRR surface or replacing $\phi = \ln \zeta$ and the mapping (5) into the simplified expression of the potential along the unit radius circular cylinder boundary as

$$V(x, y) = \frac{V_0}{\pi} \{\pi + j \ln[e^{-j\frac{\pi}{4}} \text{sn}(z', -1)]\}. \quad (7)$$

It is noted that the capacitance (2) is a p.u.h. quantity relevant to a cylinder with infinitesimal thickness, and neither accounts for the gap capacitance nor for the capacitance of the top and bottom surfaces of a cylinder of finite length and thickness. We approximate the top and the bottom capacitances assuming the same “per unit thickness” contribution as the per unit height capacitance of the inner and outer surfaces. The total surface capacitance of a split ring with height h and thickness w is therefore

$$C_{surf} = (h + w) C_{surf}^{p.u.h.} \quad (8)$$

Finally, the total capacitance of the SRR is obtained as the sum of the gap capacitance (1) and surface capacitance (8)

$$C_{tot} = C_{surf} + C_{gap}. \quad (9)$$

The estimation of the SRR resonance frequency requires the knowledge of both the capacitance and inductance of the SRR, based on the simple formula $f_r = 1/\sqrt{LC}$. However, the inductance of a square SRR can be obtained from the formulas of the inductance of a rectangular loop available in many textbooks; in particular, we will use the following expression for a rectangular loop of a conductor with a rectangular cross section:^{23,24}

$$L = \frac{\mu_0}{\pi} \left[(\ell_1 + \ell_2) \ln \left(\frac{2\ell_1\ell_2}{w+h} \right) - \ell_1 \ln \left(\ell_1 + \sqrt{\ell_1^2 + \ell_2^2} \right) - \ell_2 \ln \left(\ell_2 + \sqrt{\ell_1^2 + \ell_2^2} \right) - \frac{\ell_1 + \ell_2}{2} + 2\sqrt{\ell_1^2 + \ell_2^2} + 0.447(w+h) \right], \quad (10)$$

where ℓ_1 and ℓ_2 are the width and height of the rectangular loop, respectively, and h and w are the height and width of the conductor cross section, as in Fig. 1(a). For a square ring with side $\ell = \ell_1 = \ell_2$, and including the weighting factor $p_e = 1 - g/4\ell$ accounting for the effective perimeter of an SRR compared to that of a closed loop, the above formula becomes

$$L = p_e \frac{\mu_0}{\pi} \left\{ 2\ell \ln \left(\frac{2\ell^2}{w+h} \right) - 2\ell \ln \left[\ell(1 + \sqrt{2}) \right] - \ell + 2\ell\sqrt{2} + 0.447(w+h) \right\}. \quad (11)$$

III. NUMERICAL RESULTS

The contribution of the surface capacitance to the total capacitance is evaluated to show that it actually corresponds to a non-negligible fraction of it. The applicability and accuracy of the formulas developed are then assessed by examining the electric field and charge distributions and by comparing the resonance frequencies of sample SRR configurations provided by the theory with the corresponding values obtained by full-wave (FW) simulations with CST Microwave Studio (MS).

A. Contribution of the surface capacitance

In Fig. 2 are shown the gap, surface, and total capacitances of square SRRs with a fixed side length $\ell = 20$ mm calculated by (1), (8), and (9), respectively, at a variable size of the gap $g = 0.2/2$ mm and for different thicknesses, $w = 0.8, 1.6$ mm, and heights, $h = 5, 7.5, 10$ mm, of their metallic walls. At any height of the SRRs and for both considered conductor thicknesses, at the smallest gap sizes, the gap capacitance provides the dominant contribution, for the larger conductor the gap capacitance being as large as twice the surface capacitance, yet the surface capacitance is not negligible either. As the gap width increases, the gap capacitance decreases faster than the surface capacitance, and already for moderately wide gaps the latter contributes a larger amount to the total capacitance. The conclusion that can be drawn from the considered examples, which are indicative of a broad range of ring configurations, is that both capacitance terms need to be

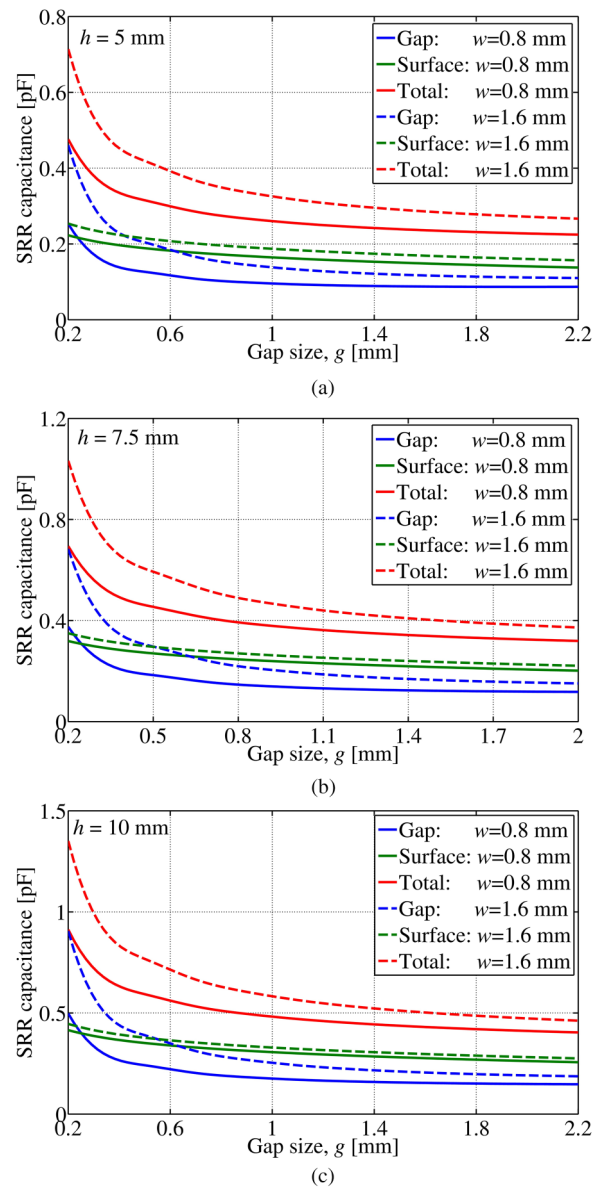


FIG. 2. Gap, surface, and total capacitances of a 3D square SRR with side $\ell = 20$ mm at variable width of the gap $g = 0.2/2$ mm for two different conductor thicknesses $w = 0.8, 1.6$ mm, and SRR heights equal to: (a) $h = 5$, (b) $h = 7.5$, and (c) $h = 10$ mm.

taken into account in the estimation of the total equivalent capacitance of 3D square SRRs.

B. Electric field and charge distribution

Next, we consider a square SRR with side $\ell = 20$ mm, gap width $g = 1$ mm, conductor thickness $w = 0.8$ mm, and height

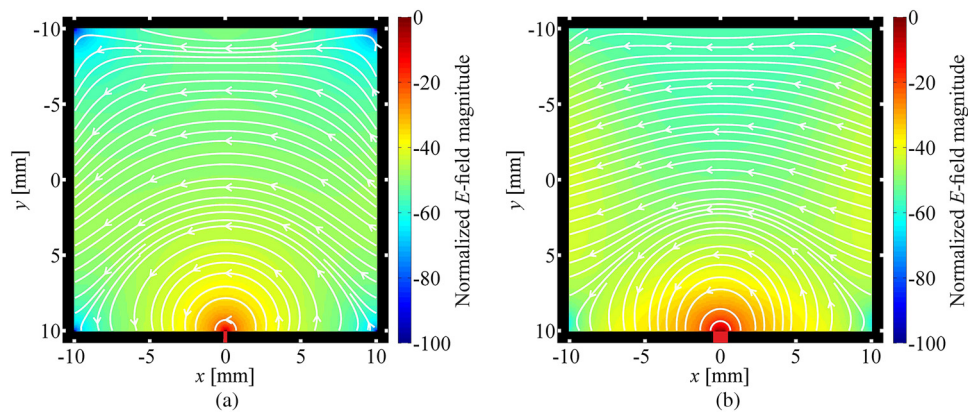


FIG. 3. (a) Field lines and maps of the normalized magnitude of the irrotational part of the electric field in the cross sections of (a) a square cylinder with side $\ell = 20$ mm and an infinitesimal gap at $(0, \ell/2)$; (b) an SRR with the same transverse size as the cylinder, but finite height $h = 5$ mm and finite gap size $g = 1$ mm. In this latter plot, the irrotational component of the electric field is extracted from the total field simulated with CST MS.

$h = 5$ mm [cf. Fig. 1(a)]. The vector plot and map of the normalized magnitude of the irrotational (electrostatic) part of the electric field for the model reference problem of an infinite cylinder with an infinitesimal gap and the same cross section of the SRR and for the actual SRR are shown in Figs. 3(a) and 3(b), respectively. The second plot is obtained by applying the Helmholtz-Hodge decomposition³³ to numerically extract the irrotational part from the total field simulated with CST MS. It is noted that while the total tangential field obviously vanishes on the metallic walls of the SRR, the irrotational part of the field does not fulfil by itself the boundary conditions and it has both normal and tangential components at the surface of the resonator. This can be observed in both plots of Fig. 3, where the field lines in the model cylinder and actual SRR exhibit very similar patterns. Some disagreement can be observed in the distribution of the field magnitude, seemingly due to both the finite width of the gap in the SRR and its finite height; however, these discrepancies are limited and localized in the rear part of the SRR, where the field magnitude is significantly smaller and the stored energy minimal.

A direct comparison of the profile of the linear charge density in two sample SRRs and in the reference cylinder is shown in Fig. 4. The SRRs have the same transverse dimensions, with $\ell = 20$ mm, $g = 2$ mm, $w = 0.8$ mm, but different heights, $h = 5$ and 10 mm; the charge densities along their cross sections have been calculated from the component of the electric field normal to the surface of the SRRs simulated with CST MS. Each curve in Fig. 4 is normalized with respect to the corresponding total charge along the cylinder or SRR cross section. In line with the field maps in Fig. 3, theoretical and FW results agree well in the front portion of the SRR cross section, with the agreement improving for the taller SRR considered; some deviation between the analytical and simulated charge densities can instead be observed in the rear portion of the SRR, where, however, the charge

tends to vanish. The capability of the analytical model developed to form a useful tool for estimating the capacitance and resonant properties of 3D square SRRs is further studied in the following sections.

C. Estimation of resonance frequency

Comparisons of analytical calculations of the resonance frequency of square SRRs with results of numerical simulations are used to demonstrate the effectiveness of the proposed expression for the 3D square SRR surface capacitance. We refer again to one of the ring configurations considered previously, with the SRR having side length $\ell = 20$ mm, conductor thickness $w = 0.8$ mm, and different heights $h = 5, 7.5,$

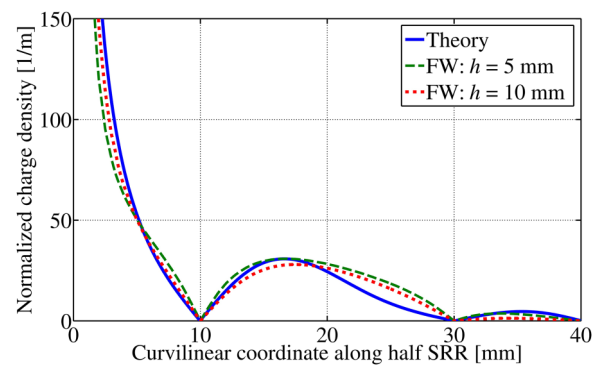


FIG. 4. Normalized linear charge density along the curve γ [cf. Fig. 1(a)] corresponding to one half of the cross section of an SRR with side $\ell = 20$ mm, gap $g = 2$ mm, and conductor thickness $w = 0.8$ mm. Normalization is with respect to the total charge along the cross section. Theoretical results for the infinite square cylinder are compared with FW simulation results for finite SRRs with height $h = 5, 10$ mm.

10 mm, while the width of the gap is assumed as a variable parameter. In the simulations performed with CST MS, the SRR material was set to be copper. The resonance frequency has been determined for the gap width ranging from

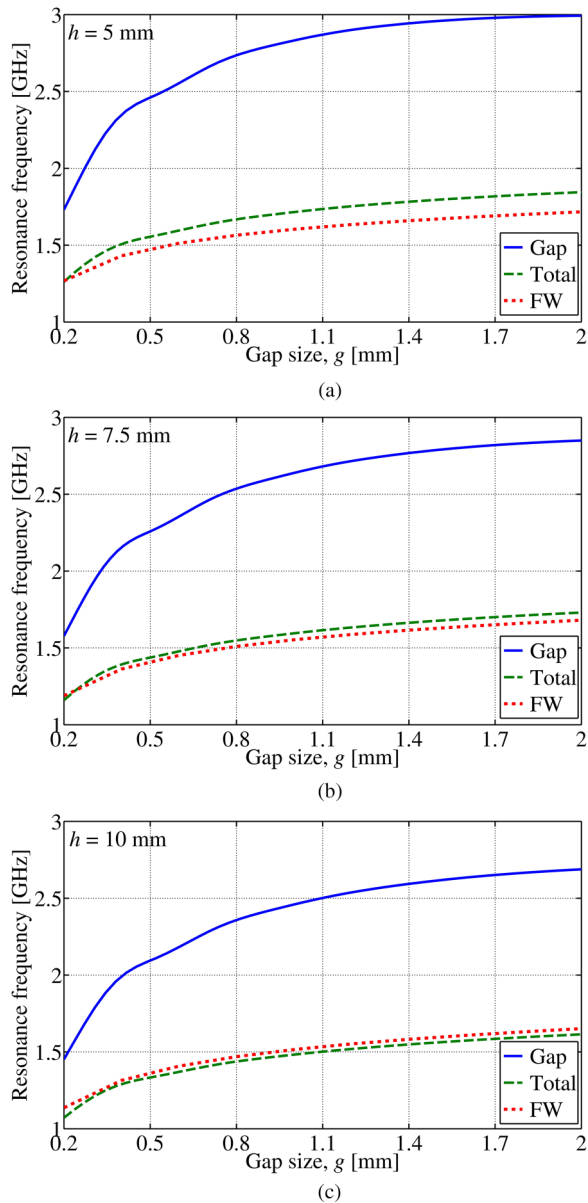


FIG. 5. Resonance frequencies of square SRRs with internal side $\ell = 20$ mm, conductor thickness $w = 0.8$ mm, for variable gap width and different SRR heights $h = 5, 7.5, 10$ mm. The analytical estimations considering only the gap capacitance (i.e., disregarding the surface capacitance, blue lines) and including both the gap and surface capacitances (green lines) are compared with the values obtained with FW simulations (red lines). (a) $h = 5$ mm; (b) $h = 7.5$ mm; (c) $h = 10$ mm.

0.2 to 2 mm. The results of analytical calculations, both disregarding and including the contribution of the surface capacitance, and numerical simulations for the resonance frequency of the SRRs are shown in Fig. 5. As apparent, taking the surface capacitance into account provides a significantly better agreement with numerical results. While the trend of the SRR resonance frequency variation against the gap size of analytical predictions is remarkably consistent with that of FW simulations for any considered SRR height, the quantitative agreement tends to improve for taller SRRs; this is presumably because those rings are closer to the ideal 2D cylindrical geometry considered for the derivation of the surface capacitance in this model and the neglected contributions from the field at the truncated ends of actual finite SRRs weight progressively less for longer SRRs.

To gain further insight into the accuracy of analytical predictions, we have also compared the values of capacitance and inductance calculated with formulas (9) and (11), respectively, with the corresponding estimations deduced from the full-wave simulation of the driving point impedance of the SRRs fed at the gap. The equivalent R, L, and C parameters of the SRRs have been determined by curve fitting, with a least square criterion, the expression of the input impedance of their equivalent circuit model, of the form shown in Fig. 1(b) but also including a resistive component placed in series with the inductance, to the corresponding quantity simulated with CST MS. These comparisons are shown in Fig. 6, from which it is apparent that the estimation of the capacitance provided by (9) becomes increasingly accurate for longer more tubular devices, while formula (11) generally leads to some overestimation of the SRR inductance, though gradually smaller for greater SRR heights. As a result, the resonance frequencies of the SRRs predicted by the proposed formulas tend to converge to marginally smaller values than those obtained with FW simulations for increasingly taller SRRs. However, these inaccuracies are in the order of just a few percentage of the SRR resonance frequencies for longer resonators, as shown also in Sec. IV.

IV. EXPERIMENTS

Experiments have been conducted to evaluate the resonance frequency of square SRRs of a variable height to compare with the corresponding analytical estimations. To identify the resonance frequency, we used the simple measurement setup schematically depicted in Fig. 7(a): the SRRs to be tested were placed over a low density balsa wood support in between two transmitting and receiving magnetic loop probes connected to a vector network analyser (VNA). The transmission coefficient s_{21} between the two probes was measured with the VNA and the position of the resonance frequency identified as that at which s_{21} exhibits a peak.

The SRRs were manufactured by mechanically slicing a copper pipe with a square cross section and cutting a vertical slit along the pipe slices to form the resonator gap.

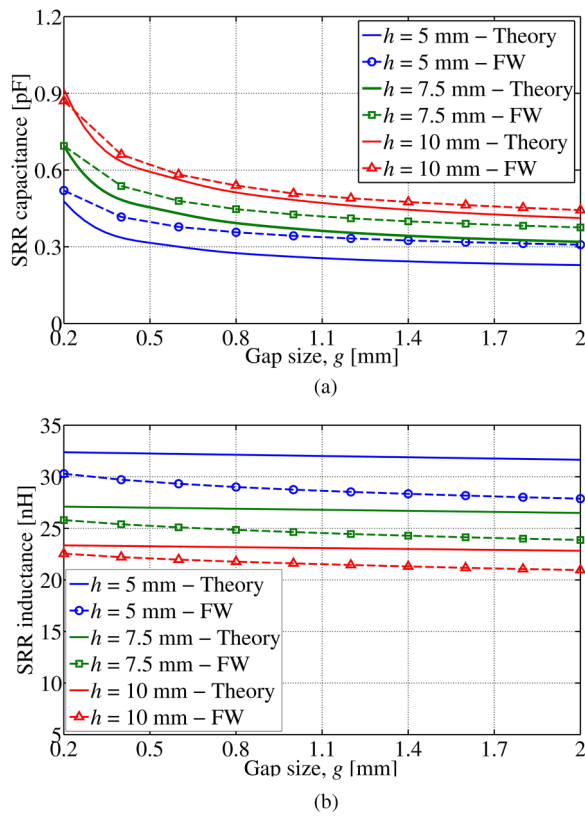


FIG. 6. Equivalent circuit parameters of square SRRs with internal side $\ell = 20$ mm and conductor thickness $w = 0.8$ mm for variable gap width and different SRR heights $h = 5, 7.5, 10$ mm. The theoretical predictions of the SRR capacitance and inductance provided by formulas (9) and (11) are compared with the corresponding numerical results derived by curve fitting the expression of the SRR input impedance associated with the equivalent circuit model in Fig. 1(b), including an additional resistive component in series with the inductance, to FW simulated impedance data: (a) capacitance; (b) inductance.

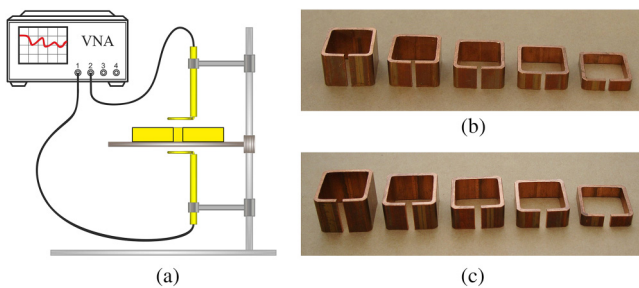


FIG. 7. (a) Schematic view of the setup for the measurement of the SRR resonance frequency. (b) Set of SRRs of different heights produced by slicing and slitting a square copper pipe with 20-mm-long external sides, copper thickness $w = 1.626$ mm, and nominal gap size $g_n = 1$ mm; (c) a second similar set of SRRs with nominal gap size $g_n = 2$ mm.

TABLE I. Comparison of the theoretical and measured values of the resonance frequencies of the copper SRRs with variable height and different gap widths shown in Fig. 7.

Nominal gap width $g_n = 1$ mm					Nominal gap width $g_n = 2$ mm				
h	Actual g (mm)	f_r (GHz)		Δf_r (%)	Actual g (mm)	f_r (GHz)		Δf_r (%)	
		Theory	Measured			Theory	Measured		
5	1.5	1.97	1.83	7.65	2.3	2.08	1.94	7.22	
8	1.56	1.83	1.78	2.81	2.26	1.93	1.884	2.44	
10	1.63	1.781	1.774	0.4	2.25	1.87	1.862	0.43	
12	1.61	1.737	1.737	0	2.35	1.84	1.853	0.7	
15	1.6	1.697	1.714	0.99	2.32	1.8	1.827	1.48	

A few sample SRRs are shown in Figs. 7(b) and 7(c). The external side length of the pipe was 20 mm and the copper thickness $w = 1.626$ mm. Two sets of split pipes with nominal gap width g_n of 1 and 2 mm and heights $h = 5, 8, 10, 12$, and 15 mm were fabricated. However, cutting the gap results in residual strain relaxation of copper which tends to widen the gap to a greater than the original cut width. The actual measured gap widths for the two sets of realized SRRs are provided in Table I along with the measured resonance frequencies f_r in comparison with the respective quantities predicted by the theory. The percentage error associated with the predicted f_r with respect to the measured data is calculated as follows:

$$\Delta f_r(\%) = \frac{|f_r^{\text{Theory}} - f_r^{\text{Measures}}|}{f_r^{\text{Measures}}} \times 100. \quad (12)$$

It is evident from Table I that analytical and measured values of f_r are in good agreement, the larger discrepancies occurring for the SRRs with the smallest height, which however are less than 8% for both considered gap widths. These errors further reduce for greater values of the SRR height. As noted in Sec. III, the fact that for the tallest SRRs, the resonance frequencies predicted analytically are slightly smaller than those measured in experiments is believed to be the combined effect of the accuracy of (9) improving for longer SRRs and the analytical inductance (11) generally providing slightly overestimated values for the equivalent L of the SRRs.

V. CONCLUSIONS

An analytical model has been presented for the fundamental mode of metallic 3D singly split square ring resonators leading to an approximate expression of the total capacitance of the SRRs expressed as the sum of the usual parallel-plate-like capacitance of the gap and an additional contribution associated with the non-uniform charge distribution on the resonators walls. It has been shown that by taking into account both these capacitance contributions to study the resonance frequency of 3D square SRRs leads to a significant improvement in the accuracy of the analytical predictions.

These predictions were shown to agree well with the results of both numerical simulations and measurements for a variety of SRR configurations. The proposed model also provides expressions for the charge and current mode distributions, whose knowledge enables the calculation of the interaction energy between 3D square SRRs and thereby of their electric and magnetic coupling constants, which in turn are sufficient to predict the performance of an arbitrary collection of resonators. The related investigation of the influence of the specific geometry and relative orientation of the SRRs on their electric and magnetic interactions, to gain the insight required for the design and development of realistic metamaterial structures and other devices, is beyond the scope of this paper and will be addressed in a separate work. It is noted that the proposed approach can be easily extended to rectangular and polygonal SRRs by adopting different conformal mappings. Furthermore, due to the linearity of the problem, the analytical expressions derived for singly split resonators can be extended in a straightforward manner to the case of multigap resonators by simply superimposing the contributions associated with each gap.

ACKNOWLEDGMENTS

Support for this work was provided by the Engineering and Physical Sciences Research Council (EPSRC) (Grant No. EP/N010493/1) as part of the SYMETA project (www.symeta.co.uk).

APPENDIX A: POTENTIAL AND CAPACITANCE p.u.h. IN A SQUARE CONDUCTING CYLINDER WITH A FINITE GAP APERTURE

By following the steps outlined in Ref. 34, the potential function associated with the irrotational part of the electric field in a one-turn infinite circular cylindrical coil with radius R , driven by a voltage V_0 applied across a pair of plane parallel electrode plates spaced a finite distance g apart, can be derived in the form of a Fourier series as

$$\Phi(r, \phi) = \frac{V_0}{\pi} \sum_{n=1}^{\infty} \frac{1}{n^2} \left(\frac{r}{R}\right)^n \sin\left(\frac{n\alpha}{2}\right) \sin(n\phi), \quad (\text{A1})$$

where $0 \leq r \leq R$, $0 < \phi < 2\pi$, and $\alpha = 2R \arcsin[g/(2R)]$ denotes the angle subtended by the gap opening in the coil. It is easy to note that for $\alpha \rightarrow 0$ (A1) reduces to the simpler Fourier series solution for the potential in a circular cylindrical coil with an infinitesimal gap, which can be found for example in Ref. 35

$$\Phi(r, \phi) = \frac{V_0}{\pi} \sum_{n=1}^{\infty} \frac{1}{n} \left(\frac{r}{R}\right)^n \sin(n\phi). \quad (\text{A2})$$

From a computational point of view, it would be desirable to rewrite (A1) into a closed form. Setting $\zeta = (r/R)e^{j\phi}$ and replacing the trigonometric terms with their exponential counterparts, (A1) can be brought into the form

$$\Phi(r, \phi) = -\frac{V_0}{\alpha\pi} \operatorname{Re} \left\{ \sum_{n=1}^{\infty} \frac{1}{n^2} \left[(\zeta e^{j\frac{\alpha}{2}})^n - (\zeta e^{-j\frac{\alpha}{2}})^n \right] \right\}, \quad (\text{A3})$$

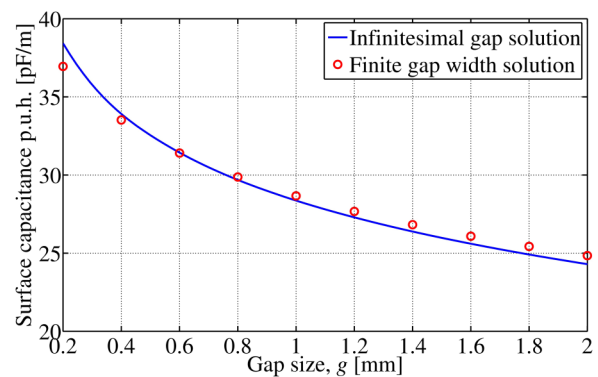


FIG. 8. Surface capacitance p.u.h. of a cylinder with square cross section with side $\ell = 20$ mm for variable gap width g . The values of the capacitance p.u.h. calculated by referring to the expressions of the field and potential in a cylinder with an infinitesimal gap are compared with those obtained from the potential function (16) that takes into account a finite width of the gap.

which can be actually expressed in terms of the dilogarithmic function³⁶ as

$$\Phi(r, \phi) = -\frac{V_0}{\alpha\pi} \operatorname{Re} [Li_2(\zeta e^{j\frac{\alpha}{2}}) - Li_2(\zeta e^{-j\frac{\alpha}{2}})]. \quad (\text{A4})$$

In passing it is noted that (A2) can be similarly reduced to the closed form (3). The conformal map (5) can be applied into (A4) to obtain the potential inside a conducting cylinder with a square cross section and a finite gap aperture, and from that, in the way outlined in Sec. II, the electric field and the surface charge density can be derived to calculate the capacitance p.u.h. of the cylinder as according to (2). This quantity has been calculated by using both solutions for a square cylinder with an infinitesimal and a finite gap, and the two sets of results are compared in Fig. 8. It can be seen that employing the solution for an infinitesimal gap provides values of the capacitance p.u.h. of the reference square cylinder very similar to those obtained starting from the potential (A4) taking into account a finite gap width; this comes essentially as a result of the capacitance integral (2) being only extended over the actual cross section of the SRR also when the solution for an infinitesimal gap is used, i.e., the portion of the charge density existing in the gap is discarded. Although the solution for a finite gap cylinder does not appear to make a substantial difference in the calculation of the capacitance for the range of considered SRR gap widths, while involving some added analytical complexity, it might possibly turn useful to describe resonators with very large gaps, like for example U-shaped structures.³⁹

APPENDIX B: ELECTRIC FIELD AND CHARGE AND CURRENT DENSITIES IN A SQUARE CONDUCTING CYLINDER

Using the complex properties of Jacobi elliptic functions,^{37,38} the potential function for a square cylinder (6) can be explicitly written as

$$u(x, y) = \frac{V_0}{\pi} \operatorname{atan}[f(x', y')] = \frac{V_0}{\pi} \operatorname{atan} \left[\frac{\operatorname{cn}(y', 2) [\sqrt{2} \operatorname{cn}(y', 2) - \operatorname{cn}(x', -1) \operatorname{dn}(x', -1) \operatorname{sn}(y', 2)]}{\operatorname{dn}(y', 2) \operatorname{sn}(x', -1) - \operatorname{cn}(x', -1) \operatorname{cn}(y', 2) \operatorname{dn}(x', -1) \operatorname{sn}(y', 2)} - \frac{\operatorname{sn}(x', -1) [\operatorname{dn}(y', 2) + \sqrt{2} \operatorname{sn}(x', -1) \operatorname{sn}^2(y', 2)]}{\operatorname{dn}(y', 2) \operatorname{sn}(x', -1) - \operatorname{cn}(x', -1) \operatorname{cn}(y', 2) \operatorname{dn}(x', -1) \operatorname{sn}(y', 2)} \right], \quad (\text{B1})$$

where $(x', y') = [\operatorname{Re}(z'), \operatorname{Im}(z')] = (x - y, x + y) \Gamma^2(1/4) / (4\ell\sqrt{2\pi})$, from the definition of z' given after Eq. (6), and $\operatorname{cn}(z, k)$ and $\operatorname{dn}(z, k)$ are the Jacobi cosine and delta amplitude elliptic functions. For the electric field, from (B1) we then have

$$\mathbf{E}_1 = -\nabla u = - \left[\left(\frac{\partial u}{\partial x'} \frac{\partial x'}{\partial x} + \frac{\partial u}{\partial y'} \frac{\partial y'}{\partial x} \right) \hat{\mathbf{x}} + \left(\frac{\partial u}{\partial x'} \frac{\partial x'}{\partial y} + \frac{\partial u}{\partial y'} \frac{\partial y'}{\partial y} \right) \hat{\mathbf{y}} \right] - \frac{\Gamma^2(1/4)}{4\ell\sqrt{\pi}} \frac{1}{\sqrt{2}} \left[\left(\frac{\partial u}{\partial x'} + \frac{\partial u}{\partial y'} \right) \hat{\mathbf{x}} + \left(-\frac{\partial u}{\partial x'} + \frac{\partial u}{\partial y'} \right) \hat{\mathbf{y}} \right], \quad (\text{B2})$$

where

$$\begin{aligned} \frac{\partial u}{\partial x'} = \frac{V_0}{\pi} \frac{1}{1 + f^2(x', y')} \{ & \sqrt{2} \operatorname{cn}(x', -1) \operatorname{dn}(x', -1) \operatorname{dn}(y', 2) [\operatorname{cn}^2(x', -1) \operatorname{sn}^2(y', 2) - 1] \\ & + 2 \operatorname{cn}(y', 2) \operatorname{sn}(y', 2) \{ \operatorname{dn}(y', 2) [\operatorname{sn}^4(x', -1) + 1] + \sqrt{2} \operatorname{sn}(x', -1) [1 - \operatorname{cn}^2(y', 2) \operatorname{dn}^2(x', -1)] \} \} \\ & \cdot [\operatorname{dn}(y', 2) \operatorname{sn}(x', -1) - \operatorname{cn}(x', -1) \operatorname{cn}(y', 2) \operatorname{dn}(x', -1) \operatorname{sn}(y', 2)]^{-2}, \end{aligned} \quad (\text{B3})$$

$$\begin{aligned} \frac{\partial u}{\partial y'} = \frac{V_0}{\pi} \frac{1}{1 + f^2(x', y')} \{ & \operatorname{cn}(x', -1) \operatorname{dn}(x', -1) \{ \sqrt{2} \operatorname{dn}(y', 2) - [1 + \operatorname{dn}^4(y', 2)] \operatorname{sn}(x', -1) \} \\ & + \sqrt{2} \operatorname{cn}(y', 2) \operatorname{sn}(x', -1) \operatorname{sn}(y', 2) \{ 1 + [2 \operatorname{cn}^2(x', -1) - 3] \operatorname{dn}^2(y', 2) \} \\ & - \sqrt{2} \operatorname{sn}^2(y', 2) [\operatorname{cn}^3(x', -1) \operatorname{dn}(x', -1) \operatorname{dn}(y', 2) + 2 \operatorname{cn}(y', 2) \operatorname{sn}(y', 2) \operatorname{sn}^3(x', -1)] \} \\ & \cdot [\operatorname{dn}(y', 2) \operatorname{sn}(x', -1) - \operatorname{cn}(x', -1) \operatorname{cn}(y', 2) \operatorname{dn}(x', -1) \operatorname{sn}(y', 2)]^{-2}. \end{aligned} \quad (\text{B4})$$

The linear charge density to be used in (2) is simply related to the normal component of the electric field as follows:

$$\rho(\gamma) = \epsilon_0 E_{1n} = \begin{cases} -\epsilon_0 E_{1x}, & x = \ell/2, \quad g/2 \leq y \leq \ell/2, \\ -\epsilon_0 E_{1y}, & -\ell/2 \leq x \leq \ell/2, \quad y = \ell/2, \\ \epsilon_0 E_{1x}, & x = -\ell/2, \quad 0 \leq y \leq \ell/2. \end{cases} \quad (\text{B5})$$

The current density can be deduced from the charge density by using the current continuity equation. However, the normalized current density, whose knowledge, as mentioned in Sec. I, can be instrumental for the analytic calculation of the magnetic coupling between 3D square SRRs,²⁷ can be simply obtained by composing the corresponding function for circular SRRs²⁷ $J_n(\phi; \phi_g) = 1 - \log[\sin(\phi/2)] / \log[\sin(\phi_g/2)]$, where ϕ_g denotes the angular opening of half of the SRR gap, with the conformal map (5); thereby, the resulting current tapering function is

$$J_n(z) = 1 - \frac{\log \left[\sqrt{\frac{1}{2} \{ 1 - \operatorname{Re}[e^{-j\frac{\pi}{2}} \operatorname{sn}(z', -1)] \}} \right]}{\log \left[\sqrt{\frac{1}{2} \{ 1 - \operatorname{Re}[e^{-j\frac{\pi}{2}} \operatorname{sn}(z'_g, -1)] \}} \right]}, \quad (\text{B6})$$

where $z'_g = z_g e^{j\frac{\pi}{4}} \Gamma^2(1/4) / (4\ell\sqrt{\pi})$ and $z_g = \ell/2 + jg/2$ is the coordinate in the z -complex plane of the square SRR ends at the

gap. It is noted that the charge density amplitude could be directly derived by taking the divergence of (B6) as according to the current continuity equation: $\rho_n \sim j\omega^{-1}(\nabla \cdot \mathbf{J}_n)$. The theoretical current tapering given by (B6) is compared in Fig. 9 with the

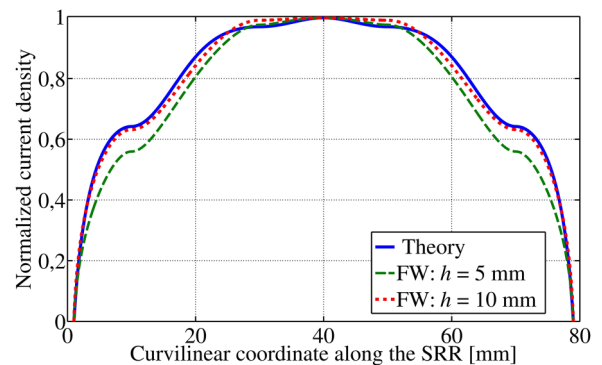


FIG. 9. Normalized linear current density along the curve γ [cf. Fig. 1(a)] corresponding to the cross section of an SRR with side $\ell = 20$ mm, gap width $g = 2$ mm, and conductor thickness $w = 0.8$ mm. The theoretical expression (22) is compared with FW simulation results of the linear current density along the mid cross section of 3D square SRRs with heights $h = 5, 10$ mm.

current along the cross sections of two 3D square SRRs with height $h = 5$ and $h = 10$ mm obtained from FW simulations with CST MS. A good agreement between the theoretical and numerical results for the current is observed for both considered SRRs, which confirms the applicability of the derived analytical expressions for the current and charge densities to the calculation of the coupling of 3D square SRRs by the approach previously recalled based on expressing the coupling parameters in terms of mutual electric and magnetic energies.^{26–28}

REFERENCES

- ¹D. Sjöberg, A. J. Johansson, and C. Larsson, “Electromagnetic properties of heterogeneous material structures produced in 3D-printers,” in *2014 International Conference on Electromagnetics in Advanced Applications (ICEAA)* (IEEE, Palm Beach, 2014), pp. 605–607.
- ²D. Espalin, D. Muse, E. MacDonald, and R. Wicker, “3-D printing multifunctionality: Structures with electronics,” *Int. J. Adv. Manuf. Tech.* **72**(5), 963–978 (2014).
- ³S.-Y. Wu, C. Yang, W. Hsu, and L. Lin, “3D-printed microelectronics for integrated circuitry and passive wireless sensors,” *Microsyst. Nanoeng.* **1**, 15013 (2015).
- ⁴M. Wajih Elsallal, J. Hood, and I. McMichael, “3D printed material characterization for complex phased arrays and metamaterials,” *Microw. J.* **59**(10), 20–34 (2016).
- ⁵F. Castles, D. Isakov, A. Lui, Q. Lei, C. E. J. Dancer, Y. Wang, J. M. Janurudin, S. Speller, C. Grovenor, and P. S. Grant, “Microwave dielectric characterization of 3D-printed BaTiO₃/ABS polymer composites,” *Sci. Rep.* **6**, 22714 (2016).
- ⁶Y. Xie, S. Ye, C. Reyes, P. Sithikong, B. I. Popa, B. J. Wiley, and S. A. Cummer, “Microwave metamaterials made by fused deposition 3D printing of a highly conductive copper-based filament,” *Appl. Phys. Lett.* **110**(18), 1–5 (2017).
- ⁷E. S. Rosker, R. Sandhu, J. Hester, M. S. Goorsky, and J. Tice, “Printable materials for the realization of high performance RF components: Challenges and opportunities,” *Int. J. Antennas Propagat.* **2018**, 9359528 (2018).
- ⁸D. R. Smith, J. B. Pendry, and M. C. K. Wiltshire, “Metamaterials and negative refractive index,” *Science* **305**(5685), 788–792 (2004).
- ⁹K. Aydin, I. Bulu, K. Guven, M. Kafesaki, C. M. Soukoulis, and E. Ozbay, “Investigation of magnetic resonances for different split-ring resonator parameters and designs,” *New J. Phys.* **7**(1), 168 (2005).
- ¹⁰O. Sydoruk, E. Tatartschuk, E. Shamonina, and L. Solymar, “Analytical formulation for the resonant frequency of split rings,” *J. Appl. Phys.* **5**, 014903 (2009).
- ¹¹R. S. Penciu, K. Aydin, M. Kafesaki, T. Koschny, E. Ozbay, E. N. Economou, and C. M. Soukoulis, “Multi-gap individual and coupled split-ring resonator structures,” *Opt. Express* **16**, 18131–18144 (2008).
- ¹²S. Zahertar, A. D. Yalcinkaya, and H. Torun, “Rectangular split-ring resonators with single-split and two-splits under different excitations at microwave frequencies,” *AIP Adv.* **5**(11), 117220 (2015).
- ¹³I. Al-Naib, C. Jansen, and M. Koch, “Thin-film sensing with planar asymmetric metamaterial resonators,” *Appl. Phys. Lett.* **93**(8), 083507 (2008).
- ¹⁴M. J. Freire, R. Marqués, F. Medina, M. A. G. Laso, and F. Martín, “Planar magnetoinductive wave transducers: Theory and applications,” *Appl. Phys. Lett.* **85**(19), 4439–4441 (2004).
- ¹⁵R. A. Shelby, D. R. Smith, S. C. Nemat-Nasser, and S. Schultz, “Microwave transmission through a two-dimensional, isotropic, left-handed metamaterial,” *Appl. Phys. Lett.* **78**(4) (2001).
- ¹⁶F. Driscoll, G. O. Andreev, D. N. Basov, S. Palit, T. Ren, J. Mock, S.-Y. Cho, N. M. Jokerst, and D. R. Smith, “Quantitative investigation of a terahertz artificial magnetic resonance using oblique angle spectroscopy,” *Appl. Phys. Lett.* **90**(9), 092508 (2007).
- ¹⁷A. Vallecchi, C. Stevens, and E. Shamonina, “3D coupled resonators for enhanced filter design,” in *12th European Conference on Antennas and Propagation (EuCAP 2018)*, London, UK, 9–13 April 2018 (IET, 2018).
- ¹⁸J. D. Baena, J. Bonache, F. Martín, R. Marqués, F. Falcone, T. Lopetegui, M. A. G. Laso, J. García-García, M. F. Portillo, and M. Sorolla, “Equivalent-circuit models for split-ring resonators and complementary split-ring resonators coupled to planar transmission lines,” *IEEE Trans. Microw. Theory Tech.* **MTT-53**, 1451–1461 (2005).
- ¹⁹R. Marqués, F. Mesa, J. Martel, and F. Medina, “Comparative analysis of edge- and broadside-coupled split ring resonators for metamaterial design—Theory and experiment,” *IEEE Trans. Antennas Propagat.* **51**(10), 2572–2581 (2003).
- ²⁰F. Bilotti, A. Toscano, and L. Vegni, “Design of spiral and multiple split-ring resonators for the realization of miniaturized metamaterial samples,” *IEEE Trans. Antennas Propagat.* **55**, 2258–2267 (2007).
- ²¹Z. Nehari, *Conformal Mapping* (Dover Publications, New York, 1975).
- ²²J. E. Allen and S. E. Segre, “The electric field in single-turn and multi-sector coils,” *Nuovo Cimento* **21**, 980–987 (1961).
- ²³F. W. Grover, *Inductance Calculations: Working Formulas and Tables* (Instrument Society of America, Research Triangle Park, NC, 1981).
- ²⁴L. Shatz and C. Christensen, “Numerical inductance calculations based on first principles,” *PLoS One* **9**(11), e111643 (2014).
- ²⁵V. Delgado, O. Sydoruk, E. Tatartschuk, R. Marqués, M. J. Freire, and L. Jelinek, “Analytical circuit model for split ring resonators in the far infrared and optical frequency range,” *Metamaterials* **3**, 57–62 (2009).
- ²⁶L. D. Landau and E. M. Lifschitz, *Electrodynamics of Continuous Media* (Pergamon, Oxford, 1984).
- ²⁷E. Tatartschuk, N. Gneiding, F. Hesmer, A. Radkovskaya, and E. Shamonina, “Mapping inter-element coupling in metamaterials: Scaling down to infrared,” *J. Appl. Phys.* **111**, 094904 (2012).
- ²⁸N. Gneiding, O. Zhuromskyy, E. Shamonina, and U. Peschel, “Circuit model optimization of a nano split ring resonator dimer antenna operating in infrared spectral range,” *J. Appl. Phys.* **116**, 164311 (2014).
- ²⁹E. Shamonina, V. A. Kalinin, K. H. Ringhofer, and L. Solymar, “Magnetoinductive waves in one, two, and three dimensions,” *J. Appl. Phys.* **92**, 6252–6261 (2002).
- ³⁰M. Shamonin, E. Shamonina, V. A. Kalinin, and L. Solymar, “Resonant frequencies of a split-ring resonator: Analytical solutions and numerical simulations,” *Microw. Opt. Technol. Lett.* **44**(2), 133–136 (2005).
- ³¹G. A. Rinard and G. R. Eaton, *Biomedical EPR—Part B: Methodology, Instrumentation, and Dynamics* (Kluwer, New York, 2005), Chap. 2, pp. 19–52.
- ³²L. M. Milne-Thomson, “Jacobian elliptic functions and theta functions,” in *Handbook of Mathematical Functions with Formulas, Graphs, and Mathematical Tables*, edited by M. Abramowitz and I. A. Stegun, 9th printing (Dover, New York, 1972), Chap. 16, pp. 567–581.
- ³³H. Bhatia, G. Norgard, V. Pascucci, and P. Bremer, “The Helmholtz-Hodge decomposition—A survey,” *IEEE Trans. Vis. Comput. Gr.* **19**(8), 1386–1404 (2013).
- ³⁴H. A. Haus and J. R. Melcher, *Electromagnetic Fields and Energy* (Prentice-Hall, Englewood Cliffs, NJ, 1989), Chap. 10, Example 10.1.2, pp. 418–419.
- ³⁵N. Takeuchi and K. Sugita, “Potential distributions in a single-turn theta pinch coil,” *Jpn. J. Appl. Phys.* **20**(7), 1327–1328 (1981).
- ³⁶I. A. Stegun, “Dilogarithm,” *Handbook of Mathematical Functions with Formulas, Graphs, and Mathematical Tables*, M. Abramowitz and I. A. Stegun, 9th printing (Dover, New York, 1972), §27.7, pp. 1004–1005.
- ³⁷See <http://functions.wolfram.com/09.36.19.0001.01> for Re.
- ³⁸See <http://functions.wolfram.com/09.36.19.0002.01> for Im.
- ³⁹J. Zhou, T. Koschny, and C. M. Soukoulis, “Magnetic and electric excitations in split ring resonators,” *Opt. Express* **15**, 17881–17890 (2007).